



Delft University of Technology

## The MoonWEC, a new technology for wave energy conversion in the Mediterranean Sea

Miquel, A. M.; Lamberti, A.; Antonini, A.; Archetti, R.

**DOI**

[10.1016/j.oceaneng.2020.107958](https://doi.org/10.1016/j.oceaneng.2020.107958)

**Publication date**

2020

**Document Version**

Final published version

**Published in**

Ocean Engineering

**Citation (APA)**

Miquel, A. M., Lamberti, A., Antonini, A., & Archetti, R. (2020). The MoonWEC, a new technology for wave energy conversion in the Mediterranean Sea. *Ocean Engineering*, 217, Article 107958. <https://doi.org/10.1016/j.oceaneng.2020.107958>

**Important note**

To cite this publication, please use the final published version (if applicable). Please check the document version above.

**Copyright**

Other than for strictly personal use, it is not permitted to download, forward or distribute the text or part of it, without the consent of the author(s) and/or copyright holder(s), unless the work is under an open content license such as Creative Commons.

**Takedown policy**

Please contact us and provide details if you believe this document breaches copyrights. We will remove access to the work immediately and investigate your claim.



## The MoonWEC, a new technology for wave energy conversion in the Mediterranean Sea

A.M. Miquel<sup>a</sup>, A. Lamberti<sup>b</sup>, A. Antonini<sup>c</sup>, R. Archetti<sup>b,\*</sup>

<sup>a</sup> Innovation Dept., EOLOS Floating Lidar Solutions, C Segre 12, Montcada i Reixac, 08110 Barcelona, Spain

<sup>b</sup> DICAM - University of Bologna - Viale Risorgimento 2, Bologna 40136, Italy

<sup>c</sup> Faculty of Civil Engineering and Geosciences (CiTG), Delft University of Technology, Stevinweg 1, 2628 CN Delft, The Netherlands

### ARTICLE INFO

#### Keywords:

New concept  
WEC  
Mediterranean Sea  
Moonpool  
CALM  
Resonant

### ABSTRACT

This work presents the MoonWEC, a new device for wave energy conversion. This new concept encompasses several working principles as the heaving point absorber, the oscillating water column and the overtopping. The development of the new WEC has been carried out through numerical modelling. Three main parts of the device have been simulated: a hollow floating structure, a central moonpool and a CALM mooring system. All the parts of the model have been coupled to obtain the general behaviour of the device under the effect of irregular sea states. The device has been designed according to the Mediterranean Sea wave climate. Its dimensioning aims to maximize the power absorption by tuning both, device and moonpool, natural periods with the identified prevailing sea states. Six mooring system configurations have been tested in order to obtain a stable, safe and yet effective behaviour. Finally, performance indicators have been drawn to assess power production in two selected locations in the Mediterranean Sea.

### 1. Introduction

Above 2/3 of the planet surface is covered by oceans and approximately half of the world's population lives within a 100 km from the coast, this alone should place Wave Energy among the most promising energy sources within renewables. Furthermore, wave energy flux is higher than its main renewable competitors, i.e. 5 and 20 times denser than wind and solar energy, respectively, see [Twidell and Weir \(2015\)](#). According to [Møork et al. \(2010\)](#), the annual global wave energy potential is over 32.000 TWh/yr and the harvesting potential could easily cover 20% of world's electricity demand.

However, waves are not distributed uniformly throughout the oceans. The wave climate of a particular area basically depends on the meteo-climatic conditions and on the geographical characteristics of such area. Higher wave energy fluxes are found from middle to high latitudes for both hemispheres in open oceans. Reason for that is the high prevalence of winds at those latitudes and the long fetches. On the one hand, there is a predominance of higher fluxes in the western coasts of the continents; given that the global circulation pattern mainly generates westerlies. On the other hand, shielded areas such as the Baltic and Mediterranean seas, have much lower average fluxes than open oceans, despite being located at the correct latitudes. This is due to their typically small fetches.

Studies conducted by [Møork et al. \(2010\)](#), [Arinaga and Cheung \(2012\)](#), [Gunn and Stock-Williams \(2012\)](#) endorse what stated in the previous paragraph and allows to set numbers to Wave Energy potential. Wave Energy fluxes can reach 120 kW/m in the Antarctic Ocean but on average range between [40 – 80] kW/m in open ocean areas at the right latitudes. In the European Atlantic coasts, average wave power grows from 30 kW/m off Portugal to 75 kW/m in Scotland, to later get back to 30 kW/m if continuing northwards to the Norwegian coasts (see [Clément et al. \(2002\)](#), [Mollison and Pontes \(1992\)](#)). In the Mediterranean Sea the average wave energy flux is 3 kW/m. However, it strongly varies depending on the geographical location, ([Liberti et al., 2013](#)). There are two areas with significant higher average wave energy fluxes; the region between the Balearic islands and Sardinia and the channel of Sicily account with 15 kW/m and 10 kW/m, respectively. The former, results in an average of 90 MWh/m of wave energy reaching the west coast of Sardinia every year. Furthermore, a study conducted by [Vicinanza et al. \(2011\)](#), based on the analysis of the wave measuring buoys from the Italian national network and comprising over 18 years of data records determined that the two most energetic Italian locations are Alghero, in Sardinia, and Mazara del Vallo, in Sicily, with 9.1 kW/m and 4.7 kW/m, respectively. According to these numbers, seems reasonable to think that wave energy exploitation can be feasible in some areas of the Mediterranean Sea. Even more if one realizes that

\* Corresponding author.

E-mail address: [renata.archetti@unibo.it](mailto:renata.archetti@unibo.it) (R. Archetti).

<https://doi.org/10.1016/j.oceaneng.2020.107958>

Received 18 March 2020; Received in revised form 30 June 2020; Accepted 14 August 2020

Available online 29 August 2020

0029-8018/© 2020 The Authors.

Published by Elsevier Ltd.

This is an open access article under the CC BY-NC-ND license

(<http://creativecommons.org/licenses/by-nc-nd/4.0/>).

storms at this location are far less destructive than those occurring in other regions, such as the North Sea. Thus, reducing the threat for wave energy converters' survivability.

Despite wave energy conversion not fully reaching the commercial stage yet, is not a young discipline. Yoshio Masuda (1925–2009) conceived the Oscillating Water Column (OWC) converter concept. By the late 1970s, Masuda deployed at open sea the first large scale WEC, the Kaimei. Meanwhile other precursors such as McCormick (McCormick, 1974), Salter (Salter, 1974), Budall and Falnes (Falnes and Budal, 1978) were also developing novel technologies and approaches such as self-rectifying turbines, the duck or control strategies to increase the devices' efficiency. All that was fuelled when the British Government developed an ambitious R&D program on wave energy, respectively. However, in the 1980s due to oil price stabilization and a change of Government policy, the British Wave Energy Program came to a halt setting a closing date for the first generation of waves energy converters. Twenty years later, the European Commission decided to include Wave Energy in their R&D programme on Renewable Energies giving birth to the second generation of WECs such as the LIMPET prototype, built in the island of Islay, Scotland, (Whittaker et al., 2006); the Pico prototype, in the Azores Islands, Portugal, or the first integrated in breakwater WEC array, which was installed in the port of Mutriku, Spain. Also in the Mediterranean Sea several WEC prototypes reached the TRL 6–8, (Pisacane et al., 2018). There were also less successful technologies that did not reach the commercialization stage or that soon after deploying their first commercial devices did not resist the hardships of extreme storms.

Marine environment poses a huge challenge to engineering. WECs are usually fine tuned machines that work under very demanding conditions. Loads of extreme waves can reach 50 times those of the working regime. Hence, the design of a machine that needs to work for certain specifications but survive for, not frequent, but very different ones. In the long term some other effects such as fatigue, corrosion and bio fouling also add up to the technical difficulties to overcome in order to develop a successful system. These are all well known and studied phenomena by the offshore industry, the main obstacle is to overcome them at a reasonable cost that permits such technology to be competitive in a market where the majority of the competitors do not have bear with such adversities. However, technology develops fast and together with past experiences have allowed to reduce costs, monetary and time-wise, by half with respect to the big projects carried out at the beginning of the 2000s.

As no uniformity has been attained yet, different ways to catalogue the ever increasing number of devices have been established. Efficiency of the WEC depends on a large number of conditions, a recent review paper (Aderinto and Li, 2019) presents the theoretical efficiency, defined as the ratio of the power absorbed by the WEC to the available power in the ocean wave front before transferring to the PTO system, ranges between 5% to 55%, with an average at approximately 20%.

Recently, several technologies have been studied and developed to specifically match the Mediterranean wave climates. A study by Bozzi et al. (2013a,b), Miquel et al. (2014, 2017), Bozzi et al. (2017) optimized a heaving point absorber with linear generator, inspired in the Seabased device (Engström et al., 2009), for typical waves found offshore the Italian coasts, after conducting analysis on wave generation and absorption (Miquel et al., 2018). Two variants of the device were modelled, the effect the surge DoF has on the power absorption was studied and device interferences when installed in farms were investigated, concluding that at its optimal each device could produce up to 15 MWh/y. Furthermore, a few initiatives are prospering to bring wave energy conversion in Italy. The world's first full-scale prototype of a breakwater integrated overtopping WEC was installed at the harbour of Naples and it is currently undergoing testing at a TRL6, (Vicinanza et al., 2014). The ISWEC (Bracco et al., 2011), is a floating point absorber that converts the wave induced pitching motion of the hull into electricity through a gyroscope coupled to an

electric generator. Full-scale prototype tests were carried out off the coasts of Pantelleria island with a device rated power of 100 kW. The ISWEC point absorber reached now the second installation (Mattiazzo, 2019). Also, an attenuator device is being tested in Marina di Pisa and currently injecting electricity into the Italian national grid. The device, called H24-50v2, has been developed by 40south energy: it is composed by two bodies located one on top of the other and the waves induce a surging motion to the upper body while the lower one is fixed to the seabed in shallow waters. In addition, there are also two other devices currently being tested at the Port of Civitavecchia. The waveSAX (Peviani et al., 2017), developed by RSE is a compact size oscillating water column WEC. It can easily be installed in vertical wall breakwaters, it is expected to produce [6–8] MWh/y per unit and its main trait is that the wells turbine is directly installed in the water column. The other device is the well known REWEC3 (Boccotti, 2007), an U shaped OWC WEC; currently is undergoing the test phase with 17 caissons built with and an expected electricity production of 5.7 MWh/m y.

To sum up, there is a wide variety of WECs, at different development stages, accounting with different shapes, sizes and working principles competing against each other. Unlike the case of large wind turbines, one could say that for wave energy conversion the race is still open. This article presents a new concept of wave energy converter specifically designed for Mediterranean wave climates. In the next section, the concept will be introduced and described in detail. Afterwards, the mathematical model, that describes the device behaviour, the numerical methods and simulation conditions will be defined. Finally, the results obtained from the numerical simulations will be presented and substantial conclusions around them will be drawn.

## 2. The concept

The MoonWEC has been originally inspired by the OXYFLUX (Antonini et al., 2012, 2015, 2016a,b), a downwelling device to artificially oxygenate anoxic waters. This concept cannot fit in any of the previous classification systems as such but at the same it could suit more than one simultaneously. The novelty of MoonWEC is that encompasses distinct working principles as formulated in the previous section.

It is composed by two bodies, a floating structure and a PTO (possibly a Wells turbine). The floater has a hollow cylinder with its axis coincident to the structure's vertical axis. When placed into the water this cylinder is filled creating what is commonly known as a moonpool. When set under the action of waves, not only the structure is excited but so is the moonpool, creating a third virtual body. The moonpool then behaves similarly to a rigid body thus being able to reach the resonant state if well tuned. The energy conversion is supposed to be carried out by taking advantage of the relative motion between the floating structure and the moonpool. In order to maximize that relative motion, both bodies need to be resonating synchronously with completely opposite phases.

The MoonWEC, which is thought to be deployed offshore, is moored to the seabed through a particular catenary system commonly known as CALM system. Catenary systems are specially suitable for heaving WECs since they mainly block other degrees of freedom while releasing the heave mode free and thus, not interfering with energy conversion motion. Fig. 1 shows a cross section of the device. The lower plate is a damping disk which aims to introduce a phase lag between the floating structure and the moonpool oscillatory motions. Furthermore, the biconical upper shape is meant to enhance structure amplitude motion. Such shape could also stimulate the overtopping effect acting as ramp for waves to climb up the structure and discharge a certain amount of water within the moonpool. It all depends on the cone's aperture, a closed and steeper cone will decrease the amount of overtopping whereas a flatter and more open cone will have the opposite effect.

To sum up, the MoonWEC can be considered a point absorber, with oscillating body in heave and oscillating water column as major working principles. This study focuses on the structure and floating oscillating water column dynamics leaving the overtopping principle for future investigations.

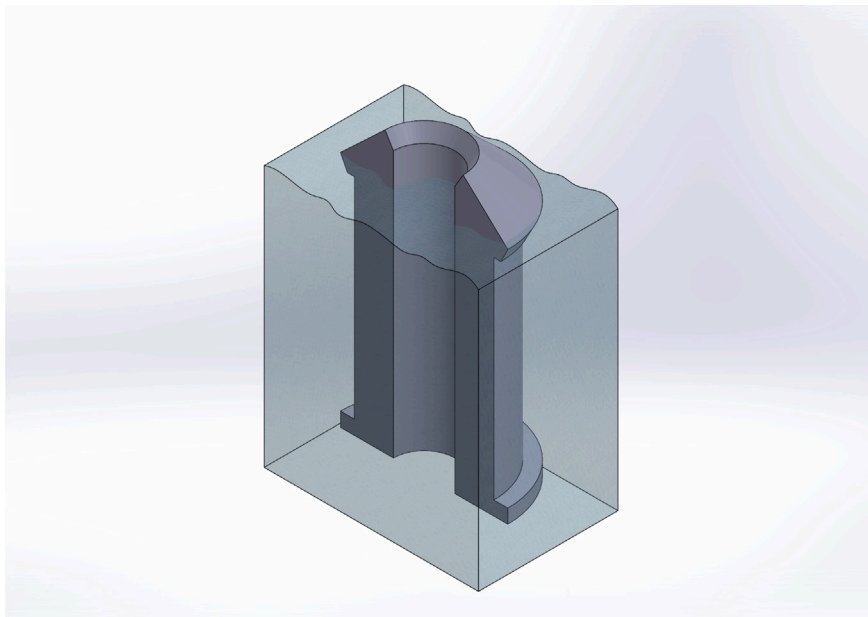


Fig. 1. CAD layout of the MoonWEC Device.

### 3. Numerical modelling

In this section, the mathematical modelling describing the WEC's dynamics and the numerical methods applied to simulate them will be thoroughly illustrated.

A model based on the potential flow theory that follows a Lagrangian approach has been developed mainly using the coding commercial software Matlab™. Fig. 2 illustrates the working scheme of the potential flow model, which follows the classical modelling architecture, i.e: the model receives a series of inputs; afterwards these inputs are processed in the model core and turned into a series of outputs. The input parameters of the model can be divided into three categories. The first class is related to the environmental conditions, which are defined by data files mainly containing time series of water surface elevation and water particle velocities. The second input class refers to the device properties, whether it be its geometrical definition, the mechanical attributes and the mooring system characteristics. Finally, the last type of inputs are the so called hydrodynamic parameters, the purpose of which is to link the environmental conditions to the body behaviour.

Each set of inputs has a specific module within the model core. Modules can communicate enabling an efficient coupling. The model then releases a series of outputs from different nature. On the one hand, the kinematics of the device, which consent to study its response to certain conditions. On the other hand, the averaged powers for that particular environmental conditions are also gathered, allowing to build the so called power matrix, capacity factor, capture width ratio, annual production and other performance indicators.

The first type of inputs, derived from the Sea conditions, are defined as regular or irregular waves based on the airy theory (Airy, 1845). In order to obtain irregular wave time series the JOSNWAP spectrum has been employed with a peak enhancement parameter equal to  $\gamma = 3.3$ , as it best represents the wave properties given at the Mediterranean Sea, (Archetti et al., 2011). In order to minimize the density energy losses when performing the Inverse Fourier Transform  $\mathcal{F}^{-1}$  the following discretization of the spectrum has been chosen:  $f = [0 : \Delta f : 3f_p]$ , where  $\Delta f = \frac{1}{t_e}$ ,  $f_p$  is the spectrum's peak frequency and  $t_e$  is the total time of the wave record, achieving a univocal correlation between the frequency and time domain. Nevertheless, since the spectrum is being truncated at  $f_{co} = 3f_p$  there is always a loss of energy related to

missing tail of the spectrum ( $3f_p - \infty$ ). An algorithm applying energy compensation used by Miquel et al. (2017) has been implemented. It is based on the ratio between the theoretical  $m_0$  and the value that comes from the numerical integration of the truncated spectrum.

The second kind of inputs are the physical parameters of the device and mooring system. That includes the structure mass and tensor of inertia, shapes, volumes and areas. As for the mooring system, the inputs are the number and type of lines, which includes their linear weight, minimum breaking load (MBL), drag coefficient and their working setup: structure fixing point, water depth, line length and horizontal anchoring point distance.

The last type of inputs are the so-called hydrodynamic parameters, i.e: the excitation force coefficient, the radiation damping coefficient and the added mass. The first explains the action of waves upon the structure and the second and third, the result of moving a body in a fluid. To compute such parameters the Boundary Element Method (BEM), based on the potential flow theory, has been applied. An open-source code named NEMOH (Babarit and Delhommeau, 2015) and developed at the LHEEA laboratory in the Ecole Centrale de Nantes, France, has been chosen to obtain the hydrodynamic parameters. Furthermore, NEMOH comes with a *suite* including also a mesher and a Matlab toolbox providing the inertia tensor of the body and the hydrostatic restoring matrix. Fig. 3 illustrates the MoonWEC surface upon which the body boundary condition is computed by the BEM method. Note that for computational efficiency reasons only half of the body is used, taking advantage of the MoonWEC's axisymmetric geometry properties.

Within the model core, the dynamic module deals with the inertial forces related to the device structure, the hydrodynamic module processes the forces interacting with the flow and the mooring module handles the effect of the mooring system. Afterwards, altogether is plugged into the general equation of motion, which is expressed in terms of the Newton's second law ( $\sum \vec{F} = m\vec{a}$ ). Each DoF of the system has its own equation of motion, since the dynamics of a certain DoF influence another DoF dynamics, different equations of motions may be linked by coupling coefficients. Therefore, when the system has more than one DoF the equations of motion are written in the matrix form, having a dimension according to the number of modelled DoF and forming a state-space system with three variables, position, velocity and acceleration, linked by time. As a result, the equation of motion system

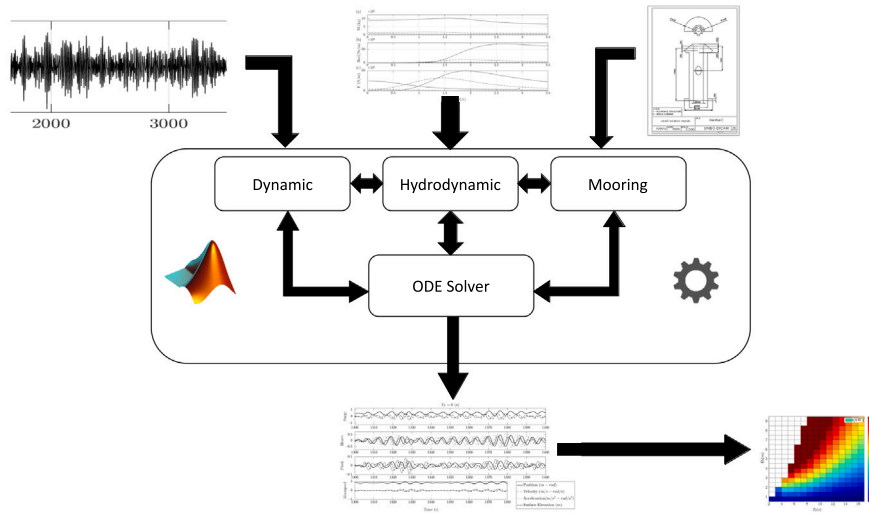


Fig. 2. Potential flow model diagram.

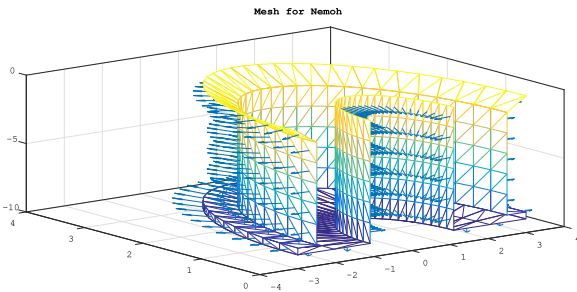


Fig. 3. Discretized MoonWEC wet surface for BEM calculations.

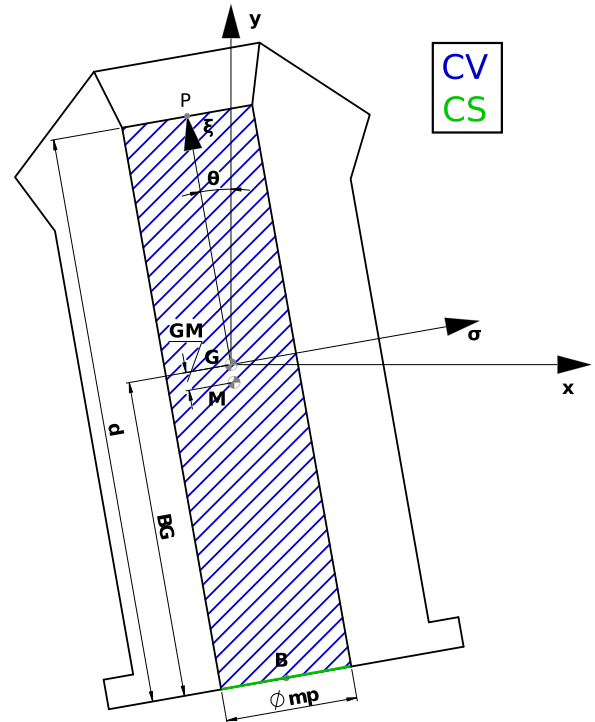


Fig. 4. Layout of the MoonWEC. In black the device structure, in blue the control volume (CV) defining the moonpool and in green the control surface (CS) of the moonpool.

becomes a system of ordinary differential equations (ODE), which has been solved following a Runge–Kutta scheme of the fifth order.

The MoonWEC has been modelled as a two-body system with four DoFs. The first body is the floating structure of the device; due to its symmetry, the body dynamics have been restricted to a single plane freeing it to move in the surge, heave and pitch modes. The second body is the water entrained in the moonpool orifice, which has been allowed to move freely only along the symmetry axis of the floating structure. Fig. 4 presents the schematic of the MoonWEC used to model the device dynamics. It has a fixed coordinate system with its origin placed at the device centre of gravity  $G$ , the axis  $(x, y)$  define the surge and heave modes respectively and the rotation in pitch is described through  $\theta$ . A moving reference system  $(\xi, \sigma)$  is set to account for the dynamics of the MoonWEC.

Following the notation in Fig. 4 Eq. (1) defines the governing expressions for the MoonWEC structure. Despite being a matrix system, for clarity all DoF have been reported separately.

$$\begin{aligned}
 (m_x + m_x^\infty)\ddot{x} + (m_{x\theta} + m_{x\theta}^\infty)\ddot{\theta} &= F_e^x(t) + F_r^x(t) + F_r^{x\theta}(t) \\
 &+ F_d^x(t) + F_{moor}^x + F_{MP}^x \\
 (m_y + m_y^\infty)\ddot{y} &= F_e^y(t) + F_r^y(t) + F_h^y(t) + F_d^y(t) + F_{moor}^y + F_{MP}^y \\
 (m_\theta + m_\theta^\infty)\ddot{\theta} + (m_{\theta x} + m_{\theta x}^\infty)\ddot{x} &= M_e^\theta(t) + M_r^\theta(t) + F_r^{\theta x}(t) \\
 &+ M_{moor}^\theta + M_{MP}^\theta + M_h^\theta(t)
 \end{aligned} \tag{1}$$

Where,  $m$  is the mass of the body,  $m^\infty$  is the added mass at  $\infty$  frequency,  $F_e(t)$  are the wave excitation forces,  $F_r(t)$  are the radiation damping forces,  $F_d(t)$  are the viscous drag forces,  $F_h(t)$  is the hydrostatic restoring force,  $F_{moor}(t)$  are the forces exerted by the mooring system

and  $F_{MP}$  and  $M_{MP}$  are the forces and moment that the moonpool applies to the MoonWEC structure.

The hydrostatic restoring force, based on the Archimedes principle yields the buoyant effect as if it was a linear spring,  $\vec{F}_h = KH\vec{z}$ , where  $KH$  is the hydrostatic stiffness matrix provided by NEMOH's toolbox and  $\vec{z}$  is the displacement of the body from the equilibrium position in a generic DoF. Besides, the wave excitation and radiation forces have been obtained from the frequency coefficients  $E(\omega)$  and  $R(\omega)$ , given by BEM method.

$$\begin{aligned}
 f_e(t) &= \frac{2}{\pi} \int_0^\infty E(\omega) \cos(\omega t) d\omega \\
 F_e(t) &= f_e(t) * \eta(t)
 \end{aligned} \tag{2}$$

$$k(t) = \frac{2}{\pi} \int_0^\infty R(\omega) \cos(\omega t) d\omega$$

$$F_r(t) = -k(t) * \dot{z}(t) - m^\infty \ddot{z}(t) \quad (3)$$

Where,  $\dot{z}(t)$  and  $\ddot{z}(t)$  are the body velocity and acceleration respectively,  $\eta(t)$  is the free surface elevation at the device axis and,  $f_e(t)$  and  $k(t)$  are the impulse response functions, used as kernels for the convolutions. Such convolutions when applying the constant delay, force the numeric algorithm to run in a fixed time step, which is equal or proportional to the delay. As a result, a substantial increase of the simulations' computational costs is obtained. Nevertheless, two alternative methods have been used. For the wave excitation force, the fact that  $\eta(t)$  is fully determined and known in advance at any given time allows to integrate it numerically regardless the chosen time step. This is not the case for the radiation damping component as  $\dot{z}(t)$  is one of the state variables and thus, an unknown. To solve it, the prony's approximation is adopted. Consisting of the substitution of the radiation damping force by a series of virtual state variables ( $F_{rd} = \sum_{i=1}^N I_i(t)$ ), allows the algorithm to run in a variable time step, more details on the prony's method are given in Diemer (1987), Hauer et al. (1990), Hauer (1991). This solution is not free and a computational cost is paid due to the increase of the system dimension to be integrated. However, the gain of getting rid of the fixed time step is larger and the overall balance in computational efficiency is positive. To ensure the maximum efficiency it is important to choose the minimum number of state variables that have a good approximation of the radiation force that delivers numerical stability. It has been observed that 6 extra  $I_i$  provide an excellent fitting without overloading excessively the system.

The last component of the hydrodynamic forces accounts for the fluid viscous effects. The drag force is formulated as part of the Morison equation and for moving bodies in oscillatory flows yields:

$$F_d = \frac{1}{2} \rho C_d A_d |u - \dot{z}|(u - \dot{z}) \quad (4)$$

Where  $\rho$  is the sea water density,  $u$  is the water particle velocities,  $\dot{z}$  is the body velocity,  $A_d$  is the cross-sectional area of the body perpendicular to the flow direction and  $C_d$  is the drag coefficient. In this study, the drag force has been decomposed according to the motion direction and the structure part. When looking at figure Fig. 1, three main parts can be identified, the upper double-cone, the central cylinder and the bottom disc. Hence, three sets of  $A_d$  and  $C_d$  have been used to compute three drag forces each one acting on a separate part. Many drag coefficient values are available in literature, in this study values from empirical experiments provided by Sadraey (2011) have been used.

To account for the dynamic behaviour of the CALM mooring system a single formula is not enough and rather a procedure is needed. Its response is highly non-linear, mainly due to the high inertia and drag of the lines. Due to the size of the lines, the induced effect on the device behaviour may not be neglected, hence both, the dynamic response of the structure and chains must be coupled. Fig. 5 shows both, a scheme of a floating platform-CALM system and a zoom of a catenary line. The expression of the mooring force for a single line is shown in Eq. (5).

$$F_{moor} = -T_0 - C_{dl} \dot{x} - m_c \ddot{x}_c \quad (5)$$

where  $T_0$  is the horizontal tension at the equilibrium position,  $C_{dl}$  is the linearized drag coefficient of the line,  $m_c$  is the mass of the chain and  $\ddot{x}_c$  is the acceleration of the chain to be added to matrix system, shown in Eq. (1). The shape equations for a catenary line are:

$$\beta = \frac{P}{T}$$

$$\beta h = \cosh(\beta l) - 1$$

$$\beta l = \sinh^{-1}(\beta l_{eff})$$

$$l_{eff} = l_T + l - l' \quad (6)$$

Where,  $\beta$  is called the shape parameter,  $T$  is the static tension of the chain,  $P$  is its linear weight,  $h$  is the water depth,  $l$  is the horizontal

distance from the fairlead in the structure and the point  $O$ , where the chain lies on the seabed and  $l_{eff}$  is the effective length of suspended chain, see Fig. 5. In these expressions  $l$ ,  $l_{eff}$  and  $T$  are unknown variables. Eq. (6) can be manipulated to obtain (7):

$$\cosh(\sqrt{(\beta h)^2 + 2\beta h} - \beta(l_T - l')) - \beta h - 1 = 0 \quad (7)$$

As this relation cannot be solved analytically, an iterative process based on a Newton–Raphson algorithm of the form (Zwillinger, 2011) has been implemented using Eq. (7) as the control function  $f(\beta_j)$ , an iterative step of  $\beta_{j+1} = \beta_j - \frac{f(\beta_j)}{f'(\beta_j)}$  and stop condition of  $|\beta_{j+1} - \beta_j| \leq \tau$ , where  $\tau$  is the tolerance. After having found  $T$ , the chain acceleration needs to be found for the ODE describing the dynamics of the platform-CALM system. From Fig. 5 the position of the chain can be derived and by applying the second time derivate the acceleration of the chain is yielded:

$$x_c = (l + x) - \beta \left( \frac{h+y}{l_{eff}} \right)$$

$$\ddot{x}_c = \ddot{x} - \ddot{\beta} \left( \frac{h+y}{l_{eff}} \right) - 2\dot{\beta} \frac{\dot{y}}{l_{eff}} - \beta \frac{\ddot{y}}{l_{eff}} \quad (8)$$

However, the chain acceleration  $\ddot{x}_c$  depends also on  $T$ , which in turn depends on the floating structure position  $(x, y)$  and thus, on the structure acceleration  $(\ddot{x}, \ddot{y})$  as well. This makes so that an integration variable of the ODE system representing the systems dynamics has a direct dependency on another integration variable  $\ddot{x}_c(\ddot{x}, \ddot{y})$ , violating the variable independence rule for ODE resolution. An approximation method of  $\ddot{x}_c$  is adopted to tackle this issue. This method, proposed by Esmailzhade and Goodarzi (2001), addresses the problematic by substituting the shape function of the catenary line by a Taylor expansion series to the second order. This allows to embed the mooring system within the MoonWECs equations of motion without needing to account the chain's acceleration explicitly. The results of the Taylor expansion and further integration to the equation of motion yield the following expression for the mooring force:

$$F_{moor} = m_{eq} \ddot{x} + C_{dl} \dot{x} + [A + 2Fy + 6Dy^2]x + Ex^3 - C\dot{x}y - G\ddot{y} \quad (9)$$

Where

$$A = P \frac{2\varphi}{\xi}; \quad F = P \left( \frac{\xi\psi + 2\eta\varphi}{\xi^3} \right)$$

$$E = P \frac{\xi\psi + 2\eta\varphi}{2\beta\xi^3} \left[ \left( \frac{\xi\psi + 2\eta\varphi}{\xi} \right)^2 - \psi^2 \right]; \quad G = \frac{A}{g}$$

$$D = P\eta \left( \frac{\xi\psi + 2\eta\varphi}{\xi^5} \right); \quad m_c = \frac{P}{g} \beta_0 \sinh\left(\frac{l}{\beta_0}\right)$$

$$m_{eq} = 2m_c - \frac{A}{g}h; \quad C = 2G$$

$$\eta = \frac{l}{\beta_0^2} \sqrt{\frac{h}{\beta_0} \left( \frac{h}{\beta_0} + 2 \right)}; \quad \xi = \frac{l-h}{\beta_0} + \frac{lh}{\beta_0^2};$$

$$\psi = \frac{l}{\beta_0^2} \left( \frac{h}{\beta_0} + 1 \right); \quad \varphi = \sqrt{\frac{h}{\beta_0} \left( \frac{h}{\beta_0} + 2 \right)}$$

To complete equation (1), only the influence of the moonpool on the MoonWEC dynamics, defined through  $F_{MP}$ , is to be accounted. Such forces, since their origin is purely inertial, are computed by means of the Newton's second law  $\sum \vec{F} = m_{MP} \vec{a}_M$ . Where,  $m_{MP}$  is the moonpool mass and  $M$  is the centre of gravity of the moonpool as shown in Fig. 4. Moonpool dynamics can be approximated as a floating cylinder with varying draft  $BG + \xi$ , as first demonstrated by Aalbers (1984). Hence,  $M$ 's position is not constant with respect to the MoonWEC varying along the  $\xi$  axis. Thus, to compute the acceleration its position must be found first. This is done by applying the definition of centre of mass to  $\|GM\|$ :

$$\|GM\| = \frac{-BG^2 + \xi^2}{2(BG + \xi)} \quad (11)$$

Now, taking the centre of gravity of the structure as reference and projecting  $GM$  onto the  $(x, y)$  axes the coordinates of the point  $M$  are obtained. Subsequently, the time derivative of such coordinates is applied twice to find the acceleration. However, the inertial forces need to be projected onto the axis  $\sigma$  to obtain the component that

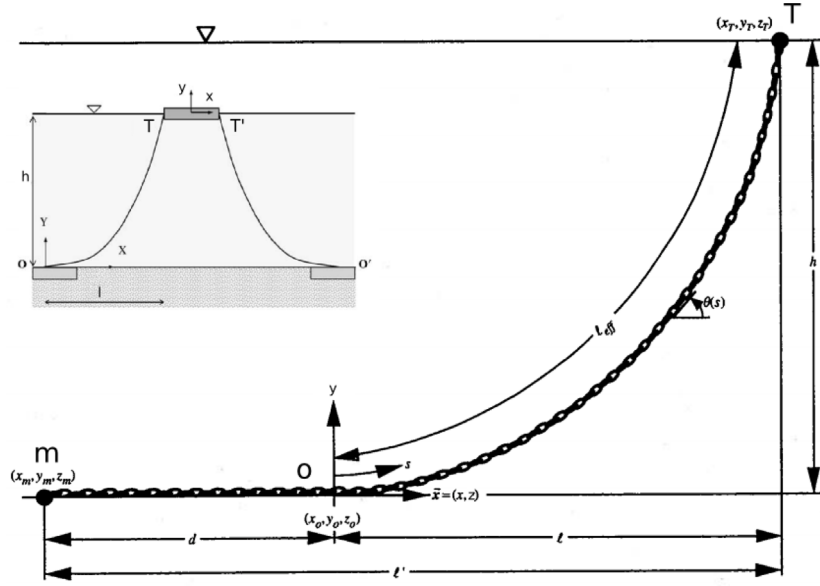


Fig. 5. Platform-CALM system and zoom of the left CALM line. Composition of figures appearing in Esmailzhade and Goodarzi (2001), DNV-GL (2010).

has an effective influence to the MoonWEC structure. Finally, an utter projection of  $F_\sigma$  back to the axes  $(x, y)$  yields the forces  $F_{MP}^x$  and  $F_{MP}^y$  in the correct reference system. Finally, the moment created by the force  $F_\sigma$  due to the distance between both gravity centres  $GM$  is obtained.

$$F_\sigma = \rho S_{mp} [(BG + \xi)(\ddot{x} - \ddot{y}\theta) + 2\xi\ddot{\xi}\theta + \frac{-BG^2 + \xi^2}{2}(\ddot{\theta} + \ddot{\xi}\theta - 2\dot{\theta}^2\theta) + \frac{1}{BG + \xi}(\ddot{\xi}\xi\theta - \dot{\xi}(\dot{\theta} + 1))] \quad (12)$$

$$\begin{aligned} F_{MP}^x &= F_\sigma \cos \theta = F_\sigma \\ F_{MP}^y &= -F_\sigma \sin \theta = -F_\sigma \theta = -\rho S_{mp} [(BG + \xi)\dot{x}\theta + \frac{-BG^2 + \xi^2}{2}(\ddot{\theta} - \frac{\dot{\xi}\theta(\dot{\theta} + 1)}{BG + \xi})] \\ M_{MP}^G &= GM F_\sigma \end{aligned} \quad (13)$$

Eqs.(13) and (26) are the result of extensive mathematical manipulation and the application of the small angle hypothesis, the full procedure can be found in Appendix.

The water motion inside a moonpool can be derived by using the deformable control volume approach, as the moonpool changes in size over time, (Liu et al., 2014; Gupta et al., 2007). Hence, the mass conservation condition must be fulfilled

$$\int_S \rho(v_{MP} - \vec{v}_S) \times \vec{n} dA = -\frac{dM_{MP}}{dt} \quad (14)$$

where  $\rho$  is the water density,  $v_{MP}$  is the velocity of the water flowing through the control surface,  $\vec{v}_S$  is the velocity of the floating structure and  $M_{MP}$  is the moonpool mass. Note that  $(v_{MP} - \vec{v}_S)$  is the relative velocity  $\vec{V}_r$  between the moonpool and the floating structure from the moonpool reference frame. The equation of motion of a moonpool is obtained by applying Newton's second law by means of the equation momentum for a deformable control volume as written in Hansen (1967):

$$\sum \vec{F} = \frac{d}{dt} \left( \int_{CV} \vec{V} \rho d\Delta \right) + \int_{CS} \vec{V} \rho (\vec{V}_r \times \vec{n}) dA = -gM_{MP} + p_i S_{mp} \quad (15)$$

Where  $\vec{V}$  is the fluid velocity in the control volume  $CV$ ,  $\vec{V}_r$  is the relative fluid velocity flowing across the control surface  $S_{mp}$ ,  $g$  is the gravity acceleration and  $p_i$  is the pressure acting on the upper side of the  $CS$ , see Fig. 4.

The force acting on the lower side of the  $CS$  can be expressed as follows:

$$F_o = \rho_o S_{mp} = F_h + F_e + F_c + F_r + F_d \quad (16)$$

Where  $F_h$ ,  $F_e$ ,  $F_r$ ,  $F_d$  and  $F_c$  have already been described in previous paragraphs and are expressed through equations (2)–(4) and (13), respectively. The pressure difference between the two sides of the control surface is the cause of the fluid acceleration. The following step is to derive the momentum equation of a deformable volume, written in Eq. (15), decomposing it for the axes  $x$  and  $y$  as  $\sum \vec{F} = (\sum F_x, \sum F_y)$ , where  $v$  turns into  $v_x$  and  $v_y$ , the horizontal and vertical velocities of the surface point of the moonpool  $P = (x_p, y_p)$ . Finally, as the moonpool axes are  $(\xi, \sigma)$ , the forces  $(\sum F_x, \sum F_y)$  are re-projected accordingly. However, the surface of the MoonWEC is considered impermeable and thus, the motion is restricted only in the  $\xi$  direction. Hence, only the  $\xi$  projection has been carried out yielding  $\sum F_\xi$ . After an extensive mathematical manipulation of equations ((14)–(16), detailedly shown in Appendix, the expressions reporting the inner and outer pressures of the  $CS$   $p_i$  and  $p_o$  are yielded:

$$p_i = \frac{\sum F_\xi}{S_{mp}} + \rho g(BG + \xi) = \rho(BG + \xi)(\dot{x}\theta + \dot{y} + \ddot{\xi} - \dot{\theta}^2\xi + g) \quad (17)$$

$$p_o = -\rho g(y - BG) + p_{rad} + p_e + p_d$$

The balance between the pressure of the two faces of the control surface  $S_{mp}$  is what drives the motion of the moonpool, and since there is no physical obstacle within both sides of  $S_{mp}$ , one can say that  $p_i - p_o = 0$ , obtaining the following moonpool equation of motion (18):

$$\begin{aligned} (p_i - p_o)S_{mp} &= \sum F_\xi + \rho g S_{mp} (y - BG) + F_d + F_r + F_e; \\ (\rho S_{mp} (BG + \xi) + m_\infty^\xi)(\ddot{\xi} + \dot{x}\theta + \dot{y}) &= f_e^\xi * \eta - \frac{1}{2} C_d^\xi S_{mp} (\dot{x}\theta + \dot{\xi})^2 - \dots \\ \dots - k^\xi * (\dot{x}\theta + \dot{\xi}) - \rho S_{mp} ((BG + \xi)(-\dot{\theta}^2\xi + g) + g(y - BG)) - m_\infty^\xi \dot{\theta}(\dot{x} - \dot{y}) \end{aligned} \quad (18)$$

where  $m_\infty^\xi$  is the added mass coefficient of the moonpool,  $C_d^\xi$  is its drag coefficient, assumed to be equal to an equivalent cylinder drag coefficient and  $k^\xi$  and  $f_e^\xi$  are the impulse response functions of the wave radiation and excitation, respectively. As seen on the previous paragraphs, the moonpool is free to move along the  $\xi$  axis. The potential model was validated through the comparison with experimental data,

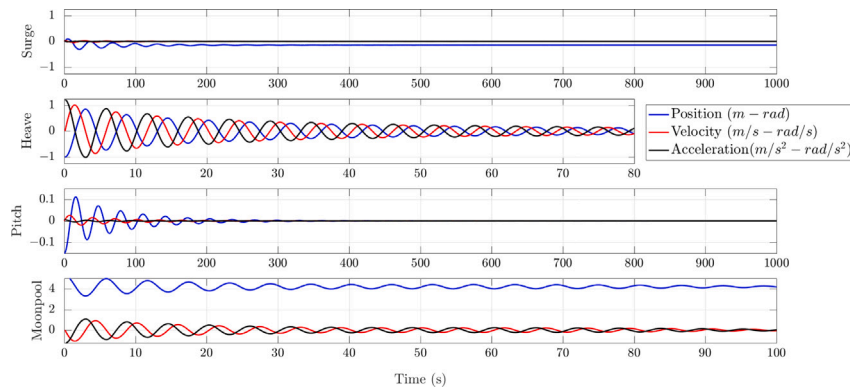


Fig. 6. Decay test results time series for the studied modes.

for a simplified case of a moored floating cylinder under regular waves and for the free decay test (Gaeta et al., 2020). The experiments were performed at the Laboratory of Hydraulic Engineering of the University of Bologna (Italy). The global dynamic response of the floating cylinder, anchored at the bottom through four catenaries, was obtained by implementing a videography analysis, which provided surge, heave and pitch motions under the tested conditions. The model results obtained for the case of free heave decay shows a good agreement with the laboratory data, reaching errors in the estimation of the natural frequency of around 0.75%.

#### 4. Dimensioning & optimization

The dimensioning, tuning and optimization of the MoonWEC can be subdivided into three categories, corresponding to each physical part of the device. Firstly, the moonpool is dimensioned; afterwards the floating structure is designed assuring its compliance with the desired conditions, hence resonance is achieved simultaneously and out of phase with the moonpool. Finally, the mooring system is dimensioned and tuned in order to modify as little as possible the device dynamics for the working conditions while preventing it from drifting away.

As shown in Sphaier et al. (2007), the natural frequency expression of a system  $\omega_0 = \sqrt{\frac{k}{m}}$  can be derived into  $\omega_0 = \sqrt{\frac{g}{d}}$  for the case of a moonpool in heave. Where  $k$  and  $m$  are the elasticity and mass of the system,  $g$  is the gravity acceleration and  $d$  is the moonpool draft. Knowing that the moonpool has to resonate for sea states around  $T_p = 6$  s, typical of sea states at the considered study sites, as will be explained later. Derivation of the moonpool draft, and in turn also the structure draft, is direct yielding  $d = 9m$ .

Having determined on a first attempt the dimensions of the moonpool, the structure wrapping the moonpool has to be sized according to the required natural frequency. In first approach, this is done by applying the Fourier transform of the linearized equation of motion (1), thus obtaining the frequency domain equation of motion:

$$F_e = X_0(-\omega^2(m + A) + i\omega B + KH) \quad (19)$$

Where  $\omega$  is the frequency of the monochromatic wave exciting the structure,  $m$  is the mass matrix of the system,  $A$  is the added mass matrix,  $B$  is the radiation damping matrix,  $KH$  is the hydrostatic stiffness matrix,  $F_e$  is the excitation force coefficient vector and  $X_0$  is the RAO, which reflects the unitary response of the system. As the draft of the structure is fixed by the moonpool constraint, the shape and diameter of the structure are the only variables left to modify. The structure has a cone shape on top in order to guarantee a smooth transition in the free surface region. Also, a damping plate has been installed at the bottom to tune the phase of the device; this effect however, cannot be modelled in the frequency domain as the drag introduced by the plate is non-linear. Therefore, the diameter of the body is the parameter upon which the RAO sensitivity analysis has

Table 1

Resonance Peak location for several structures with different main body diameters.

$D$ (m)	$\omega_0$ (rad/s)
3	1.32
4	1.22
5	1.08
6	0.9
7	0.8
8	0.66

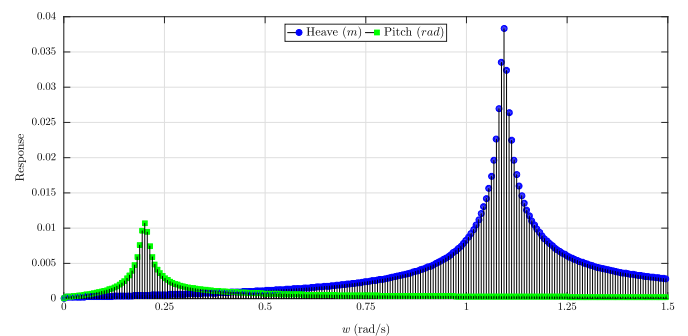


Fig. 7. Frequency domain response of the decay test for the studied modes.

been executed. Table 1 reports the resonant response peak frequency in heave of several structures with different diameters.

It is observed that for a diameter of 5 m the structure has a natural frequency of  $\omega_0 = 1.08$  rad/s, which practically coincides with most frequent  $\omega_p = 1.05$  rad/s for the selected locations of Alghero and Mazara del Vallo.

Once the preliminary frequency domain design has been completed, more detailed time domain analysis must be carried out to properly account for the non-linear effects. First step is to perform the decay or free oscillation tests. This response, measured over the time, gives the information about the natural period of the system and its damping. The chosen initial state of the device is  $IS = (x_0, z_0, \theta_0) = (0, -1, -0.15)$  using the SI units. Note that null initial displacement has been set for the horizontal dimension. It is meaningless to test the surge mode when no mooring system has been introduced, since the device will not have a reaction force aiming to bring it back to the equilibrium position. The dynamic response over time of the system is shown in Fig. 6 for the modelled DoFs. Fourier analysis is adopted to highlight the natural frequencies of the system, results are reported in Fig. 7.

No anomalies are observed in Fig. 6, the heave and pitch modes show symmetrical oscillations damped at different rates. The moonpool has an offset of the mean oscillatory position to comply with

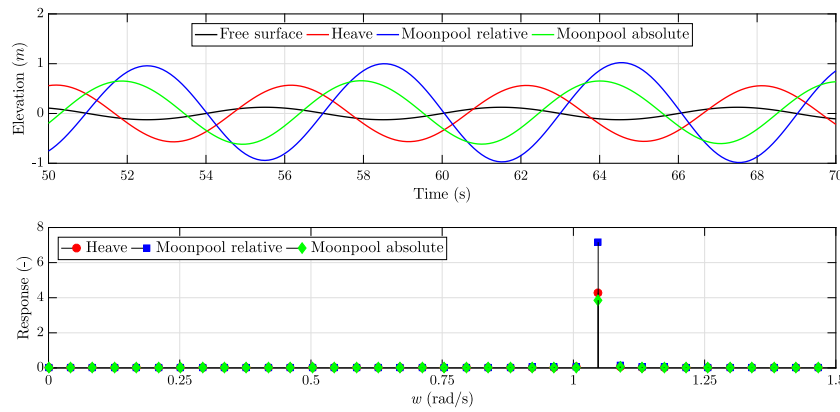


Fig. 8. Time and frequency domain response under the influence of a monochromatic wave of period  $T = 6$  s, for the heave mode and moonpool absolute and relative displacements.

coordinate system introduced in Fig. 1 and thus, showing coordinate  $\xi$ . The surge mode shows small oscillations, which are the result of the cross radiation effect surge-pitch. Finally, it assumes a resting position different than zero confirming the lack of a mooring system. The frequency domain analysis, shown in Fig. 7, reveals the natural frequencies of the system. These, show very good agreement with the frequency domain tests in the case of the heave and moonpool modes, 1.1 (rad/s). The pitch mode also shows a peak at 0.2 (rad/s), such frequency corresponds to a very long wave, practically at the limit of the linear wave theory. Thereby, for survivability the dynamics of the device at that particular frequency must be studied.

Despite the decay test provides full description of the natural device's frequencies, the identification of the phase shift between the device and the moonpool cannot be achieved. To such purpose the forced oscillation tests are carried out by bringing the device under the action of a monochromatic wave of  $H = 0.5$  m and  $T = 6$  s.

In Fig. 8 the device heave displacement and the absolute and relative (to the structure) moonpool displacements are plotted. After performing the phase analysis of the responses with respect to the free surface; the delays found for the structure, the absolute and relative displacements of the moonpool are respectively:  $\delta_h = 38.3^\circ$ ,  $\delta_{Ma} = 151.8^\circ$  and  $\delta_{Mr} = 185.9^\circ$ . That makes a relative delay between the structure and the relative motion of the moonpool of  $\delta_r = \delta_{Mr} - \delta_h = 147.6^\circ$ .

Up to this point, the dimensioning of the moonpool and the floating structure is completed and seen to be working as expected. As far as the mooring system is concerned, six configurations with different number of lines have been studied; four with two lines (one per side of the structure) and another two with four lines (two per side of the structure). On the geometric layout of the line (see Fig. 5), only three parameters can be predefined, the total length of the line  $l_T = l_{eff} + d$ , the horizontal distance between the structure and the anchoring point  $l'$ , and the vertical distance from the fair-lead to the sea bottom  $h$ . According to He et al. (2017) the chain length is set in proportion to the water depth and it usually ranges from 3 to 6 times the depth,  $3h \leq l_T \leq 6h$ . In order to minimize the line weight, a total length of  $l_T = 3h$  has been set, taking into account that the water depth is 50 m, then  $l_T = 150$  m. Within the two-line variants, two are linked to the structure at its base and the other two at the CoG quote. The four-line variants are both bonded to the structure in the same manner, the lower fair-leads are placed at the base and the upper ones at the edge of the top cone, coinciding with the still water level at rest. Finally, two different anchoring points have been set, one at a horizontal distance  $l' = 120$  m and the other at  $l' = 135$  m, Fig. 9 illustrates the different variants.

The physical properties of the lines have been selected according to the guidelines presented in DNV-GL (2010). The spiral strand steel wire ropes have been chosen owing to their superior properties. More

Table 2  
Geometric properties of CALM system configurations.

#	# of lines	$l'$ (m)	$h$ (m)	$l_r$ (m)	$l_s$ (m)	$T_0$ (s) Pitch	RAO (-) Pitch
0	0	-	-	-	-	31.25	27
1	2	120	41	24.3	11	21.75	36
2	2	135	41	9.3	26	17.85	11.5
3	2	120	45.8	22.8	15.8	28.75	17
4	2	135	45.8	7.8	30.8	21.75	130
5	4	$L_l$ $L_u$	120 151.8	41 50	24.3 18.8	11 25	21
6	4	$L_l$ $L_u$	135 166.7	41 50	9.3 33.8	26 17.85	78

precisely, a model having a nominal diameter  $\varnothing = 76$  mm, a minimum breaking load of 5647 kN and a submerged nominal weight of 23.8 kg/m.

Subsequently, decay tests of the full system (device and mooring) have been carried out for each of the six variants and results have been studied. As expected, the response in heave suffers very little variation with respect to the CALM configuration, having a natural period around  $T_0 = 6$  s and a RAO about 4. On the other hand, the mooring system increases the stiffness of the system for the pitch mode, changing its natural period  $T_0$  and RAO notably. To provide an effective comparison, the results have been summarized in Table 2, also for the unmoored system, named variant #0. The left side states the main characteristics of the chosen mooring configurations described in the previous paragraph, including the maximum displacements before the lines go slack and taut. Furthermore, the natural periods and RAOs of the overall system in pitch are shown.

Whereas a general reduction of the natural period in pitch with respect to the variant #0 is detected, no clear trend is observed for the RAO with strong variations depending on the mooring configuration. Through the results presented in Table 2 variant #3 is identified as the most convenient, with the combination of the second most reduced RAO, even more than that of variant #0, and the largest natural period  $T_0 = 28.75$  (s), the closest to variant #0 too. The aim is to minimize the pitch mode to avoid some undesired effects such as Mathieu resonance, horizontal induced loads in the structure, sloshing or uneven flow in the moonpool. Hence, mooring system variant #3 has been selected as the optimal mooring configuration for the MoonWEC.

## 5. Results

In the following paragraphs a thorough study of the behaviour of variant #3 is presented. Following the same procedure as with the unmoored device (variant #0). Firstly, the analysis shows the free

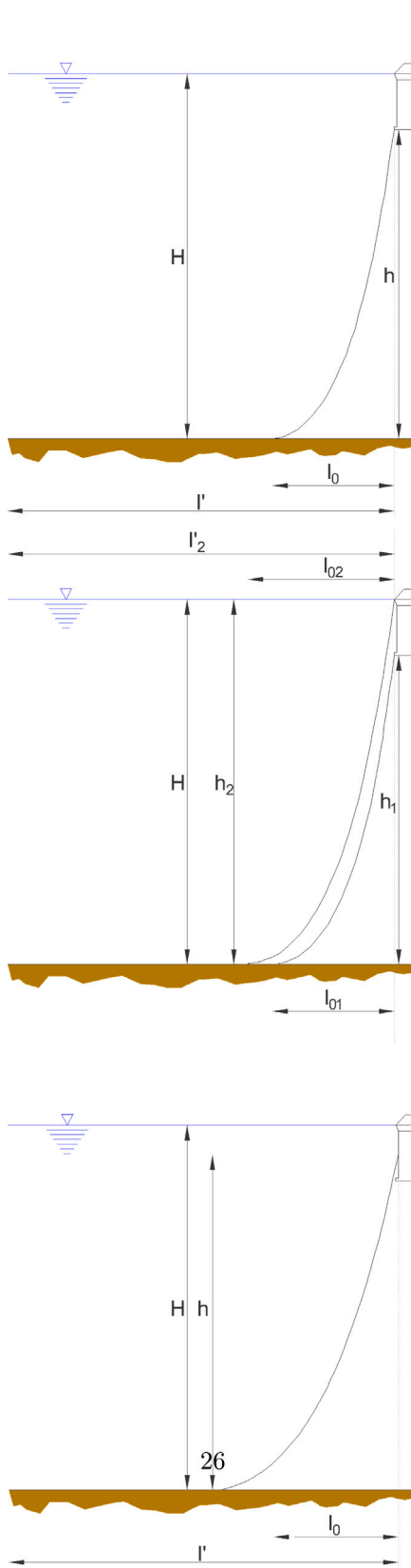


Fig. 9. Geometric CALM system layouts.

decay tests, this time including the surge mode. Figs. 10 and 11 show the results in the time and frequency domains, respectively.

It is revealed that the heave mode and the moonpool maintain the same response as in the unmoored device. For pitch mode, a minimal variation of the natural frequency is observed with respect to the device with no mooring, passing from  $T_0^p = 31.25$  s to  $T_0^p = 28.75$  s. The surge mode presents a strong correlation with the pitch mode, presenting a peak at the pitch's natural frequency and a very low natural frequency, meaning that the device tends to set back to the equilibrium position in a slow and smooth way. As no relevant differences are detected for the heave mode, the forced oscillation analysis has been carried out with a monochromatic wave with a period equal to the pitch's natural period.

Fig. 12 shows the expected behaviours, a large peak for the pitch mode, as it is resonating, a unitary response of the heave mode, as the wave period is far larger than its natural period and a damped response for the surge mode since its natural period is larger than the wave's period. The moonpool presents no response for such frequency, meaning that it moves accordingly with the floating structure and hence no relative motion is generated. A small perturbation is detected at the moonpool natural period given by the cross-correlation with the pitch mode. Finally, the device performance is simulated for the range of sea states characterizing the wave climate given at the selected locations; Alghero and Mazara del Vallo, in the western coasts of Sardinia and Sicily, respectively. That range comprehends waves from 3 to 12 s of Peak Period and 0.5 to 4.5 m of Significant Wave Height. The length of the simulations is set to 1000 waves per sea state as it is considered that the energy of the JONSWAP spectrum is fully represented by such length.

Fig. 13 shows the non-dimensional spectra of the device displacements in all modes under four irregular waves, with  $H_{m0} = 1$  m and  $T_p$  ranging from 4 to 10 s. Normalization has been carried out according to the peak parameters of the wave spectra; the wavelength for the surge, the tangent of wave steepness (in rad) for the pitch and the wave amplitude for the heave and moonpool modes.

Results show the expected behaviour for all modes. Surge displacements are reduced when compared to the wavelength proving the desired effect of the mooring system of keeping the device in place. A very similar trend is observed for the pitch mode as the mooring closely links both modes as already seen in Figs. 10 and 11. The heave mode presents resonance around the device natural frequency and as foreseen; following the free water surface for larger peak periods, (c) & (d) in Fig. 13, and damping its response for lower peak periods, (a) in Fig. 13. Finally, the moonpool mode presents a very interesting behaviour; not only by having a larger response, which means that the out-phasing of the system works, but also being able to keep an amplification factor of 3 even if the simulated sea state lies well over the natural period of the device. Fig. 14 displays an extract of the time series of figure Fig. 13(b) showing the dynamics of the system in SI units to provide a better physical awareness to Fig. 13.

Finally, the power captured by the WEC is to be estimated. While some PTO systems have been considered, this study focuses on the amount of mechanic power hold in the moonpool by its relative motion with respect to the floating structure, hereinafter referred to as net power. Following the notation from Fig. 4, the net power is calculated with the classic relation  $P(t) = F_{MP}(t)\dot{\xi}(t)$ , where  $F_{MP}(t)$  is the moonpool equivalent force, obtained from the 2nd Newton's law  $F_{MP}(t) = m_{MP}(t)\ddot{\xi}(t)$ : where  $m_{MP}(t)$  is the moonpool mass, which is time varying due to the deformable volume condition and computed as  $m_{MP}(t) = \rho g S_{mp}(BG + \xi(t))$ , being  $\rho$  the sea water density and  $g$  the gravity acceleration.

Subsequently, for each simulated sea state the instantaneous power has been computed following the above described procedure and the average value has been placed in the net power matrix, a bi-variate matrix with respect to the significant wave height and the peak period. Furthermore, the capture width ratio, which is the ratio of the absorbed

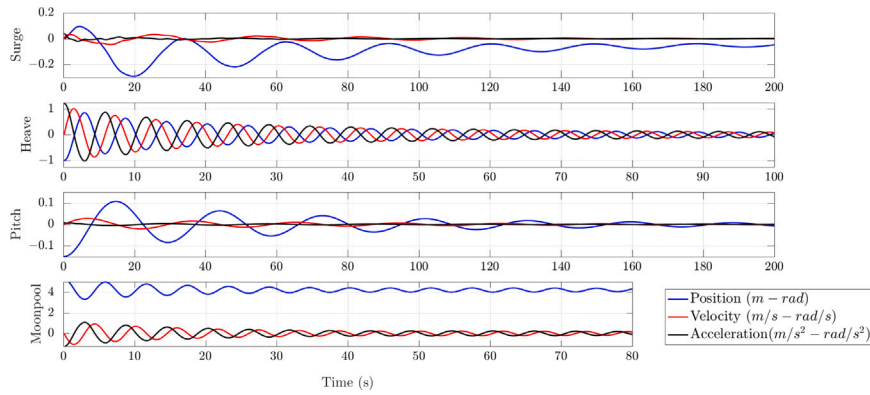


Fig. 10. Decay test time series of the MoonWEC for the studied modes.

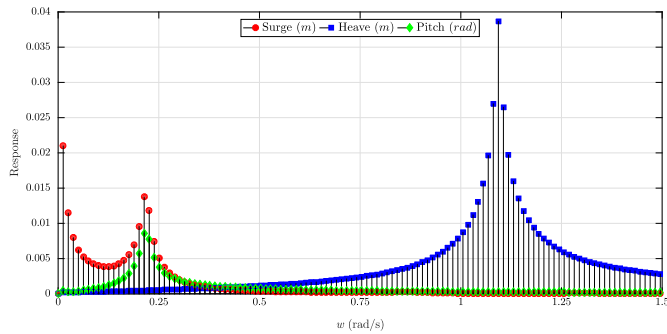


Fig. 11. Frequency domain response of the decay test of the MoonWEC for the studied modes.

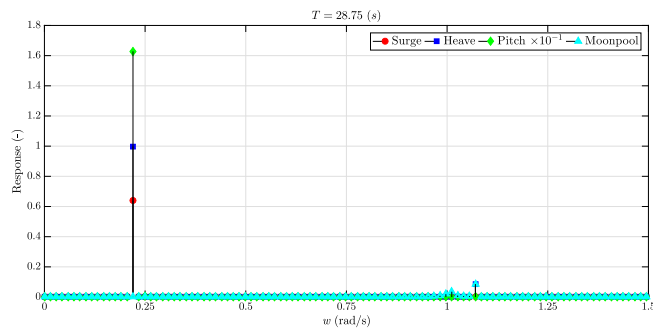


Fig. 12. Non-dimensional frequency domain response for the studied modes of the MoonWEC under the influence of a monochromatic wave of period  $T = 28.75$  s.

power and the wave energy flux has been computed in the non dimensional form using the moonpool diameter as non-dimensionalizing parameter. Results are presented in Figs. 15 and 16, respectively.

In both figures, the resonant region is clearly observed around  $T_p = 6$  s, the design resonant period, confirming what the previous analysis stated, in which power absorption by the moonpool is maximized under the most frequent conditions at Alghero and Mazara del vallo. The MoonWECs net rated power and maximum CWR amount to 18 kW and 90%, respectively. Crossing these data with the wave climates at the selected location allows to obtain site-specific performance indicators, such as the Annual Energy Production (AEP), the Average Power Absorption (P), the Mean Capture Width Ratio (CWR) and the Capacity Factor (CF). Such indicators have been computed for the selected locations, Alghero and Mazara del Vallo and summarized in Table 3.

Table 3

Performance indicators at the deployment locations.

	AEP (MWh/yr)	P (kW)	CWR (%)	CF (%)
Alghero	36	4.1	41.9	22.8
Mazara del Vallo	33.5	3.8	44.3	21.8

## 6. Conclusions

This paper aims to present a new device for wave energy conversion named The MoonWEC. This new concept, mixing several working principles is targeted to the Mediterranean Sea and its wave climate. Its technical feasibility is explored via numerical modelling. A numerical model based on the potential flow theory has been set. The code allows parallel computing and implements several tools to improve its computational efficiency. The model, simulates the response of the WEC under the influence of irregular sea states in the time domain. The MoonWEC is composed by three main elements: a hollow floating structure, a central moonpool, and a CALM mooring system; all of them simulated dynamically.

The first step in the MoonWEC's development process consists in the determination of the general dimensions of the device through the frequency domain tests. The optimal draft, for which the moonpool resonates at the established period of  $T = 6$  s is  $d = 9$  m. The draft of the moonpool is equivalent to the draft of the structure. Furthermore, frequency domain tests also show that the external diameter of the structure must be  $\varnothing = 5$  m in order to achieve resonance for that period.

Time domain tests, aimed to define more precisely the dimensional parameters of the device, reveal good agreement with the results obtained in the frequency domain tests, defining the natural periods of the device in heave and pitch,  $T_0^h = 6$  s and  $T_0^p = 31.5$  s, respectively. Whereas resonance in heave is the main dimensioning target, resonance in pitch is a rather undesired effect. Extra elements, such a disc at the bottom and a cone at the top, have been added to the structure in order to create a phase lag between the structure and the moonpool. By increasing the phase between the two parts of the device, their relative motion is amplified, thus maximizing the power absorption.

Afterwards, the mooring system of the device has been designed. Six different configurations have been tested. A description of the different variants is provided in Table 2 and Fig. 9. Results show that all variants have very little influence on the heave mode. Also, it is found that the most pre-tensioned schemes reduce considerably the natural period in pitch, taking it to a dangerous region where it may likely be excited during stormy events. Regarding the connection point to the structure, the best performance is achieved when the mooring is attached at the level of the structure's CoG, having very little influence in the pitch mode as well. However, further investigation should be done in the future at that step, since until now free surface elevation has been

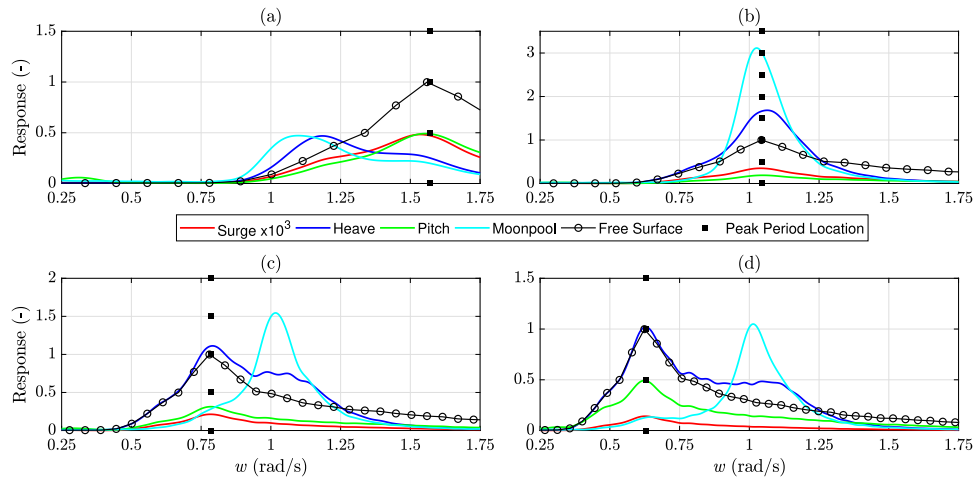


Fig. 13. Non-dimensional Spectra of the MoonWEC studied modes response to irregular wave sea states. a) for peak period  $T_p = 4$  s, (b) for peak period  $T_p = 6$  s, (c) for peak period  $T_p = 8$  s and (d) for peak period  $T_p = 10$  s.

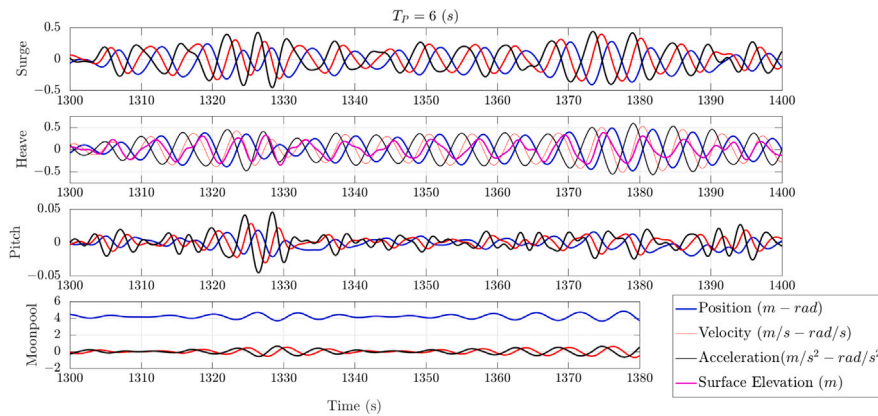


Fig. 14. Time series of the MoonWEC response for the studied modes under the influence of an irregular wave sea state with peak period  $T_p = 6$  s.

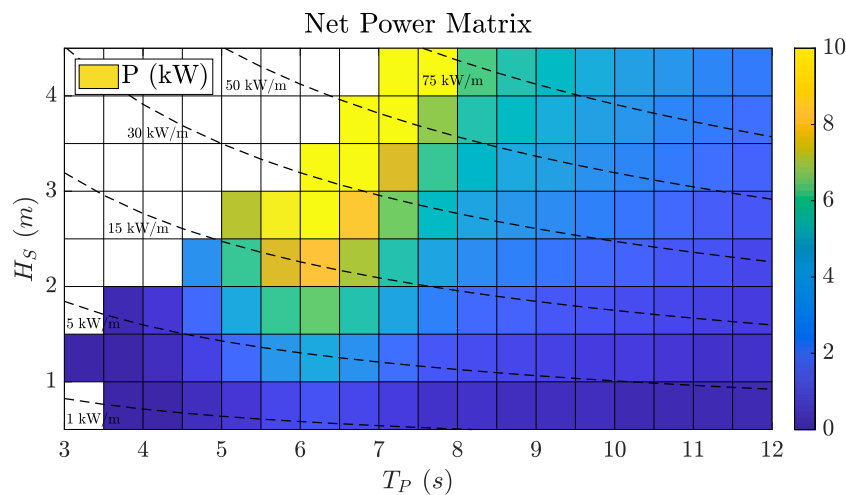


Fig. 15. Net Power Matrix for the MoonWEC device.

modelled according to the linear wave theory. Loads may increase drastically due to non-linearity of waves and stormy free surfaces have a non-linear behaviour as non-linearity increases with steepness.

In Fig. 15, the net power is shown. That is, the wave energy absorbed by the moonpool, which shows higher rates around the natural period in heave  $T_0^h = 6$  s and a rated power of 18 kW backing the

design procedure followed until now. Furthermore, the performance of the device in two of the most promising locations in the Mediterranean Sea, Alghero and Mazara del Vallo, has been assessed, as shown in Table 3. These site-specific indicators suggest electricity production is feasible, since in the energy chain, they represent the available power to the eventual PTO system that effectively generates electricity.

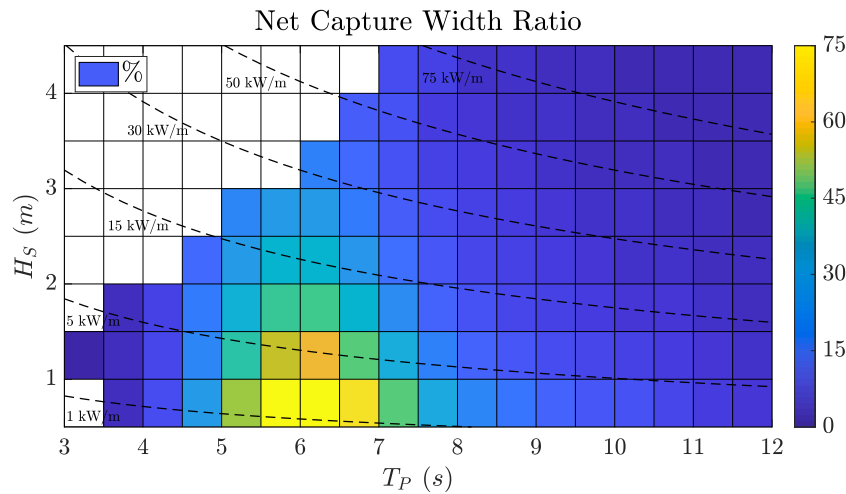


Fig. 16. Net Capture Width Ratio Matrix for the MoonWEC device.

Currently few highly efficient PTO's, such as a wells turbine or an elastomeric material PTO can be considered as future developments in this regard. According to the world Energy Council (Enerdata), the average electricity consumption of an Italian household is 2.4 MWh/yr, hence a single MoonWEC could feed 15 households. If deployed in arrays the MoonWEC could provide electricity to remote islands which lack of energy resources.

#### CRediT authorship contribution statement

**A.M. Miquel:** Conception and design of study, Acquisition of data, Analysis and/or interpretation of data, Drafting the manuscript, Revising the manuscript critically for important intellectual content. **A. Lamberti:** Analysis and/or interpretation of data, Drafting the manuscript. **A. Antonini:** Analysis and/or interpretation of data, Drafting the manuscript, Revising the manuscript critically for important intellectual content. **R. Archetti:** Conception and design of study, Acquisition of data, Analysis and/or interpretation of data, Drafting the manuscript, Revising the manuscript critically for important intellectual content, Funding.

#### Declaration of competing interest

No author associated with this paper has disclosed any potential or pertinent conflicts which may be perceived to have impending conflict with this work. For full disclosure statements refer to <https://doi.org/10.1016/j.oceaneng.2020.107958>.

#### Appendix A

As seen on the previous paragraphs, the moonpool is free to move along the  $\xi$  axis. Nevertheless, the relative motion is blocked along the  $\sigma$  axis by means of the structure walls. This exerts a considerable influence in the MoonWEC dynamics as stated in Eq. (1) through  $F_{MP}^x$  and  $F_{MP}^y$ . Such forces, since their origin is purely inertial, are computed by means of the Newton's second law:

$$\sum \vec{F} = m_{MP} \vec{a}_M \quad (20)$$

Where,  $m_{MP}$  is the moonpool mass, which has been obtained from Eq. (31) and  $M$  is the centre of gravity of the moonpool. As a result of the deformable volume condition, the point  $M$  (Fig. 4) is not static with respect to the MoonWEC and its position varies along the  $\xi$  axis. Thus, to compute the acceleration its position must be found first. This is done by applying the definition of centre of mass, which is no

other than a weighted average along the  $\xi$  axis, yielding the following distance  $\|GM\|$ :

$$\|GM\| = \frac{-BG^2 + \xi^2}{2(BG + \xi)} \quad (21)$$

Now, taking the centre of gravity of the structure as reference and projecting  $GM$  onto the  $(x, y)$  axes the coordinates of the point  $M$  are obtained. Subsequently, the time derivative of such coordinates is applied twice to find the acceleration and after some mathematical manipulation and the application of the small angle hypothesis the following relations are found:

$$x_M = x + \frac{-BG^2 + \xi^2}{2(BG + \xi)} \sin \theta \quad (22)$$

$$y_M = y + \frac{-BG^2 + \xi^2}{2(BG + \xi)} \cos \theta$$

$$\begin{aligned} \frac{dx_M}{dt} = v_{xM} &= \dot{x} + \frac{1}{(BG + \xi)} [\xi \dot{\xi} \sin \theta + \frac{-BG^2 + \xi^2}{2} (-\frac{\dot{\xi} \sin \theta}{(BG + \xi)} + \cos \theta \dot{\theta})] \\ \frac{dy_M}{dt} = v_{yM} &= \dot{y} + \frac{1}{(BG + \xi)} [\xi \dot{\xi} \sin \theta - (-BG^2 + \xi^2) (\frac{\dot{\xi} \cos \theta}{(BG + \xi)} + \dot{\theta} \sin \theta)] \end{aligned} \quad (23)$$

$$\begin{aligned} \frac{dv_{xM}}{dt} = a_{xM} &= \ddot{x} + \frac{1}{(BG + \xi)} [\xi^2 \ddot{\theta} + \ddot{\xi} \xi \dot{\theta} + 2\xi \dot{\xi} (\dot{\theta} - \frac{\dot{\xi}}{BG + \xi}) + \dots \\ &\dots + \frac{-BG^2 + \xi^2}{2} (\frac{\ddot{\xi} \dot{\theta}}{BG + \xi} + \dot{\theta}^2 + \ddot{\theta} - \frac{\dot{\xi}}{BG + \xi} (\dot{\theta} + 1 - \frac{2\dot{\xi} \dot{\theta}}{BG + \xi}))] \\ \frac{dv_{yM}}{dt} = a_{yM} &= \ddot{y} + \frac{1}{(BG + \xi)} [\xi^2 \ddot{\theta} + \ddot{\xi} \xi - 2\xi \dot{\xi} (\dot{\theta} + \frac{\dot{\xi}}{BG + \xi}) - \dots \\ &\dots - \frac{-BG^2 + \xi^2}{2} (\ddot{\theta} - \dot{\theta}^2 + \frac{1}{(BG + \xi)} (\ddot{\xi} - 2\xi \dot{\xi} (\dot{\theta} + \frac{\dot{\xi}}{BG + \xi})))] \end{aligned} \quad (24)$$

Substituting the accelerations into Eq. (20) the forces at the point  $M$  are found. However, these need to be projected onto the axis  $\sigma$  to obtain the component that has an effective influence to the MoonWEC structure. Finally, an utter projection of  $F_\sigma$  back to the axes  $(x, y)$  yields the forces  $F_{MP}^x$  and  $F_{MP}^y$  in the correct reference system:

$$\begin{aligned} F_x &= \rho S_{mp} (BG + \xi) a_{xM} \\ F_y &= \rho S_{mp} (BG + \xi) a_{yM} \end{aligned} \quad (25)$$

$$F_\sigma = F_x \cos \theta - F_y \sin \theta = F_x - F_y \theta$$

$$\begin{aligned} F_\sigma &= \rho S_{mp} [(BG + \xi) (\ddot{x} - \ddot{y} \theta) + 2\xi \dot{\xi} \dot{\theta} + \frac{-BG^2 + \xi^2}{2} (\ddot{\theta} + \ddot{\xi} \theta - 2\dot{\theta}^2 \theta \\ &\quad + \frac{1}{BG + \xi} (\ddot{\xi} \dot{\theta} - \dot{\xi} (\dot{\theta} + 1)))] \end{aligned} \quad (26)$$

$$\begin{aligned}
F_{MP}^x &= F_\sigma \cos \theta = F_\sigma \\
F_{MP}^y &= -F_\sigma \sin \theta = -F_\sigma \theta = -\rho S_{mp} [(BG + \xi) \ddot{x} \theta + \frac{-BG^2 + \xi^2}{2} (\ddot{\theta} \theta - \frac{\dot{\xi} \theta (\dot{\theta} + 1)}{BG + \xi})]
\end{aligned} \quad (27)$$

Finally, there is only one term left to fully define the dynamic influence of the moonpool upon the MoonWEC. It is the moment created by the force  $F_\sigma$  due to the distance between both gravity centres  $GM$ , obtained in Eq. (21):

$$M_{MP}^G = GMF_\sigma \quad (28)$$

## Appendix B

Following the deformable volume approach we have that the mass conservation must be respected as stated in Eq. (14), reproduced here for clarity:

$$\int_S \rho (v_{MP} - v_S) \times \vec{n} dA = -\frac{dM_{MP}}{dt} \quad (29)$$

Realizing that  $(v_{MP} - v_S)$  is the relative moonpool velocity  $\vec{v}_r$  and following the notation from Fig. 4, the left and right hand side of Eq. (29) can be rewritten respectively as:

$$\int_S \rho \vec{v}_r \times \vec{n} dA = \rho S_{mp} (v_{MP} \sin(\theta) - \dot{x}, v_{MP} \cos(\theta) - \dot{y}) \begin{pmatrix} -\sin(\theta) \\ -\cos(\theta) \end{pmatrix} \quad (30)$$

$$-\frac{dM_{MP}}{dt} = -\frac{d}{dt} \rho S_{mp} (BG + \xi) = -\rho S_{mp} \dot{\xi} \quad (31)$$

where  $S_{mp}$  is the area of the CS and  $BG$  is the distance from the CoG of the structure to S. Note that the MoonWEC structure CoG has been selected as the origin of the reference system. Recomposing equation (29) from Eqs. (30) and (31), applying the opportune mathematical simplifications and finally applying the small angle hypothesis, for which  $\sin \theta \simeq \theta$  and  $\cos \theta \simeq 1$ , the absolute velocity of the moonpool is yielded

$$V_{MP} = \dot{x} \theta + \dot{y} + \dot{\xi} \quad (32)$$

where the  $\dot{\cdot}$  on top of a variable expresses its time derivative  $\frac{d}{dt}$ . The following step is to derive the momentum equation of a deformable volume, written in Eq. (15), and here decomposed for the axes  $x$  and  $y$  as  $\sum \vec{F} = (\sum F_x, \sum F_y)$ :

$$\sum F_x = \frac{d}{dt} \left( \int_{CV} v_x \rho d\Delta \right) + \int_{CS} v_x \rho (\vec{V}_r \times \vec{n}) dA \quad (33)$$

$$\sum F_y = \frac{d}{dt} \left( \int_{CV} v_y \rho d\Delta \right) + \int_{CS} v_y \rho (\vec{V}_r \times \vec{n}) dA \quad (34)$$

where,  $CV$  and  $CS$  are the control volume and surface, respectively;  $v_x$  and  $v_y$  are the horizontal and vertical velocities of the surface point of the moonpool  $P = (x_p, y_p)$ , which are derived from Fig. 4:

$$x_p = x + \xi \sin \theta; \quad (35)$$

$$v_x = \frac{d}{dt} x_p = \dot{x} + \dot{\xi} \sin \theta + \dot{\theta} \xi \cos \theta$$

$$y_p = y + \xi \cos \theta; \quad (36)$$

$$v_y = \frac{d}{dt} y_p = \dot{y} + \dot{\xi} \cos \theta - \dot{\theta} \xi \sin \theta$$

By taking each term of Eqs. (33) and (34), developing them separately and then reunifying them, the final equations for  $\sum F_x$  and  $\sum F_y$  are obtained. Note that the small angle hypothesis has also been applied during this procedure:

$$\begin{aligned}
\frac{d}{dt} \left( \int_{CV} v_x \rho d\Delta \right) &= \rho S_{mp} \frac{d}{dt} ((\dot{x} + \dot{\xi} \sin \theta + \dot{\theta} \xi \cos \theta) (BG + \xi)) = \dots \\
\dots &= \rho S_{mp} (\dot{\xi} (\dot{x} + \dot{\xi} \theta + \dot{\theta} \xi) + (BG + \xi) (\ddot{x} + \ddot{\xi} \theta + \ddot{\theta} \xi + 2\dot{\theta} \dot{\xi} - \dot{\theta}^2 \xi \theta))
\end{aligned} \quad (37)$$

$$\begin{aligned}
\int_{CS} v_x \rho (\vec{V}_r \times \vec{n}) dA &= \rho S_{mp} ((\dot{x} + \dot{\xi} \sin \theta + \dot{\theta} \cos \theta) (-v_{MP} (\cos^2 \theta + \dots \\
\dots + \sin^2 \theta) + \dot{x} \sin \theta + \dot{y} \cos \theta)) &= \rho S_{mp} (-\dot{\xi} (\dot{x} + \dot{\xi} \theta + \dot{\theta} \xi))
\end{aligned} \quad (38)$$

$$\sum F_x = \rho S_{mp} ((BG + \xi) (\ddot{x} + \ddot{\xi} \theta + \ddot{\theta} \xi + 2\dot{\theta} \dot{\xi} - \dot{\theta}^2 \xi \theta)) \quad (39)$$

$$\begin{aligned}
\frac{d}{dt} \left( \int_{CV} v_y \rho d\Delta \right) &= \rho S_{mp} \frac{d}{dt} ((\dot{y} + \dot{\xi} \cos \theta - \dot{\theta} \xi \sin \theta) (BG + \xi)) = \dots \\
= \rho S_{mp} (\dot{x} (\dot{y} + \dot{\xi} - \dot{\theta} \xi \theta) + (BG + \xi) (\ddot{y} + \ddot{\xi} - \ddot{\theta} \xi \theta - 2\dot{\theta} \dot{\xi} \theta - \dot{\theta}^2 \xi \theta)) &
\end{aligned} \quad (40)$$

$$\begin{aligned}
\int_{CS} v_y \rho (\vec{V}_r \times \vec{n}) dA &= \rho S_{mp} ((\dot{y} + \dot{\xi} \cos \theta - \dot{\theta} \sin \theta) \\
(-v_{MP} (\cos^2 \theta + \sin^2 \theta) + \dots &
\end{aligned} \quad (41)$$

$$\dots + \dot{x} \sin \theta + \dot{y} \cos \theta) = \rho S_{mp} (-\dot{\xi} (\dot{y} + \dot{\xi} - \dot{\theta} \xi \theta))$$

$$\sum F_y = \rho S_{mp} ((BG + \xi) (\ddot{y} + \ddot{\xi} - \ddot{\theta} \xi \theta - 2\dot{\theta} \dot{\xi} \theta - \dot{\theta}^2 \xi \theta)) \quad (42)$$

Finally, as the moonpool axes are  $(\xi, \sigma)$ , the forces  $(\sum F_x, \sum F_y)$  are projected accordingly. However, as the surface of the MoonWEC is considered impermeable, the motion is restricted only in the  $\xi$  direction, thus only the  $\xi$  projected has been carried out, following the logic applied in the previous steps, the small angle hypothesis has been applied in this operation too:

$$\sum F_\xi = \sum F_x \sin \theta + \sum F_y \cos \theta; \quad (43)$$

$$\sum F_\xi = \rho S_{mp} (BG + \xi) (\ddot{x} \theta + \ddot{y} + \ddot{\xi} - \dot{\theta}^2 \xi)$$

## References

- Aalbers, A.B., 1984. The water motions in a moonpool. *Ocean Eng.* 11, 557–559.
- Aderinto, T., Li, H., 2019. Review on power performance and efficiency of wave energy converters. *Energies* 12 (22).
- Airy, G.B., 1845. On tides and waves. *Encyclopaedia Metrop.* 5 (192), 241–396.
- Antonini, A., Gaeta, M.G., Lamberti, A., 2012. Wave - induced devices for the oxygenation of deep layer: a physical investigation. *Coast. Eng. Proc.* 1 (33), <http://dx.doi.org/10.9753/icce.v33.management.56>.
- Antonini, A., Lamberti, A., Archetti, R., 2015. Oxyflux, an innovative wave-driven device for the oxygenation of deep layers in coastal areas: A physical investigation. *Coast. Eng.* 104, 54–68. <http://dx.doi.org/10.1016/j.coastaleng.2015.07.005>.
- Antonini, A., Lamberti, A., Archetti, R., Miquel, A.M., 2016a. CFD Investigations of OXYFLUX device, an innovative wave pump technology for artificial downwelling of surface water. *Appl. Ocean Res.* 61, 16–31. <http://dx.doi.org/10.1016/j.apor.2016.10.002>.
- Antonini, A., Lamberti, A., Archetti, R., Miquel, A.M., 2016b. Dynamic overset rans simulation of a wave-driven device for the oxygenation of deep layers. *Ocean Eng.* 127, 335–348. <http://dx.doi.org/10.1016/j.oceaneng.2016.10.016>.
- Archetti, R., Bozzi, S., Passoni, G., 2011. Feasibility study of a wave energy farm in the western Mediterranean Sea: Comparison among different technologies. In: *Proceedings of the International Conference on Offshore Mechanics and Arctic Engineering - OMAE*, vol. 5, pp. 447–452. <http://dx.doi.org/10.1115/OMAEE2011-49372>.
- Arinaga, R.A., Cheung, K.F., 2012. Atlas of global wave energy from 10 years of reanalysis and hindcast data. *Renew. Energy* 39 (1), 49–64.
- Babarit, A., Delhommeau, G., 2015. Theoretical and numerical aspects of the open source BEM solver NEMOH. In: *Proc. of the 11th European Wave and Tidal Energy Conference. EWTEC2015*, Nantes, France.
- Boccotti, P., 2007. Comparison between a u-OWC and a conventional OWC. *Ocean Eng.* 34 (5), 799–805.
- Bozzi, S., Giassi, M., Moreno Miquel, A., Antonini, A., Bizzozero, F., Grusso, G., Archetti, R., Passoni, G., 2017. Wave energy farm design in real wave climates: the Italian offshore. *Energy* 122 (C), 378–389. <http://dx.doi.org/10.1016/j.energy.2017.01.094>.
- Bozzi, S., Miquel, A.M., Antonini, A., Passoni, G., Archetti, R., 2013a. Modeling of a point absorber for energy conversion in Italian seas. *Energies* 6 (6), 3033–3051. <http://dx.doi.org/10.3390/en6063033>.

- Bozzi, S., Miquel, A.M., Scarpa, F., Antonini, A., Archetti, R., Passoni, G., Gruosso, G., 2013b. Wave energy production in Italian offshore: Preliminary design of a point absorber with tubular linear generator. In: 4th International Conference on Clean Electrical Power: Renewable Energy Resources Impact, ICCEP 2013, pp. 203–208. <http://dx.doi.org/10.1109/ICCEP.2013.6586990>.
- Bracco, G., Giorcelli, E., Mattiazzo, G., 2011. ISWEC: A gyroscopic mechanism for wave power exploitation. *Mech. Mach. Theory* 46 (10), 1411–1424.
- Clément, A., McCullen, P., Falcão, A., Fiorentino, A., Gardner, F., Hammarlund, K., Lomonis, G., Lewis, T., Nielsen, K., Petroncini, S., Pontes, M.T., Schild, P., Sjöström, B.O., Sørensen, H.C., Thorpe, T., 2002. Wave energy in Europe: current status and perspectives. *Renew. Sustain. Energy Rev.* 6 (5), 405–431.
- Diemer, F.J., 1987. A Prony Algorithm for Shallow Water (Mater's thesis). Massachusetts Institute of Technology.
- DNV-GL, 2010. Anchor Manual 2010, The guide to Anchoring. DNV-GL.
- Enerdata, <https://wec-indicators.enerdata.net>.
- Engström, J., Eriksson, M., Isberg, J., Leijon, M., 2009. Wave energy converter with enhanced amplitude response at frequencies coinciding with Swedish west coast sea states by use of a supplementary submerged body. *J. Appl. Phys.* 106 (6).
- Esmailzade, E., Goodarzi, A., 2001. Stability analysis of a CALM floating offshore structure. *Int. J. Non-linear Mech.* 36, 917–926.
- Falnes, J., Budal, K., 1978. Wave-power conversion by power absorbers. *Nor. Marit. Res.* 6, 6–11.
- Gaeta, M.G., Segurini, G., Moreno, A.M., Archetti, R., 2020. Implementation and validation of a potential model for a moored floating cylinder under waves. *J. Mar. Sci. Eng.* 8 (2), 131. <http://dx.doi.org/10.3390/jmse8020131>.
- Gunn, K., Stock-Williams, C., 2012. Quantifying the global wave power resource. *Renew. Energy* 44, 296–304.
- Gupta, H., Belvins, R., Banon, R., 2007. Effect of moonpool hydrodynamics on spar heave. In: Proc. of 27<sup>th</sup> International Conference on Offshore Mechanics and Arctic Engineering, Estoril, Portugal.
- Hansen, A.G., 1967. Fluid Mechanics. John Wiley and Sons, New York, NY.
- Hauer, J.F., 1991. Application of prony analysis to the determination of modal content and equivalent models for measured power system response. *IEEE Trans. Power Syst.* 6 (3), 1062–1068.
- Hauer, J.F., Demeure, C.J., Scharf, L.L., 1990. Initial results in prony analysis of power system response signals. *IEEE Trans. Power Syst.* 5 (1), 80–89.
- He, F., Leng, J., Zhao, X., 2017. An experimental investigation into the wave power extraction of a floating box-type breakwater with dual pneumatic chambers. *Appl. Ocean Res.* 67, 21–30.
- Liberti, L., Carillo, A., Sannino, G., 2013. Wave energy resource assessment in the Mediterranean, the Italian perspective. *Renew. Energy* 50, 938–949.
- Liu, L.Q., Zhou, B., Tang, Y.G., 2014. Study on the nonlinear dynamic behavior of deep sea spar platform by numerical simulation and model experiment. *J. Vib. Control* 10, 1528–1537.
- Mattiazzo, G., 2019. State of the art and perspectives of wave energy in the Mediterranean Sea: Backstage of ISWEC. *Front. Energy Res.* 7, <http://dx.doi.org/10.3389/fenrg.2019.00114>.
- McCormick, M.E., 1974. Analysis of a wave-energy conversion buoy. *AIAA J. Hydrodynamics* 8, 77–82.
- Miquel, A.M., Antonini, A., Archetti, R., Bozzi, S., Lamberti, A., 2017. Non-linear modelling of a heaving point absorber: The surge effect. *Int. J. Mar. Energy* 19, 95–109. <http://dx.doi.org/10.1016/j.ijome.2017.07.002>.
- Miquel, A.M., Antonini, A., Archetti, R., Bozzi, S., Passoni, G., 2014. Assessment of the surge effects in a heaving point absorber in the Mediterranean Sea. In: ASME 2014 33rd International Conference on Ocean, Offshore and Arctic Engineering, OMAE2014, June 8–13, San Francisco, California, USA, pp. 1–8. <http://dx.doi.org/10.1115/OMAE2014-23445>.
- Miquel, A.M., Kamath, A., Chella, M.A., Archetti, R., Bihs, H., 2018. Analysis of different methods for wave generation and absorption in a cfd-based numerical wave tank. *J. Mar. Sci. Eng.* 6 (2), 73. <http://dx.doi.org/10.3390/jmse6020073>.
- Mollison, D., Pontes, M., 1992. Assessing the Portuguese wave-power resource. *Energy* 17 (3), 255–268.
- Mørk, G., Kabuth, A., Pontes, M., 2010. Assessing the global wave energy potential. In: Proc., 29th International Conference on Offshore Mechanics and Arctic Engineering, pp. 447–454.
- Peviani, M., Danelli, A., Dadone, G., Dalmaso, A., 2017. WaveSAX device: design optimization through scale modelling and a PTO strategical control system. In: EGU General Assembly Conference Abstracts, vol. 19.
- Piscane, G., Sannino, G., Carillo, A., Struglia, S., 2018. Marine energy exploitation in the mediterranean region: steps forward and challenges. *Frontiers in Energy Research* 6 (109), <http://dx.doi.org/10.3389/fenrg.2018.00109>.
- Sadraey, M., 2011. Aircraft Performance. VDM Verlag.
- Salter, S., 1974. Wave power. *Nature* 249, 720–724.
- Sphaier, S.H., Torres, F.G.S., Masetti, I.Q., Costa, A.P., Levi, C., 2007. Monocolumn behavior in waves: experimental analysis. *Ocean Eng.* 1724–1733.
- Twidell, J., Weir, T., 2015. Renewable Energy Resources. Routledge.
- Vicinanza, D., Capietti, L., Ferrante, V., Contestabile, P., 2011. Estimation of the wave energy in the Italian offshore. *J. Coast. Res.* 64, 613–617.
- Vicinanza, D., Contestabile, P., Nørgaard, J.Q.H., Andersen, T.L., 2014. Innovative rubble mound breakwaters for overtopping wave energy conversion. *Coast. Eng.* 88, 154–170.
- Whittaker, B., Beattie, W., Folley, M., Boake, C., Whright, A., Osterried, M., 2006. The limpet wave power project - the first years of operation. *Renew. Energy* URL <http://web.sbe.hw.ac.uk/staffprofiles/bdgsa/shsg/Documents/2004sem/limpet.PDF>.
- Zwillinger, D., 2011. CRC Standard Mathematical Tables and Formulae.